Journal of Colloid and Interface Science 652 (2023) 1609–1619

Contents lists available at ScienceDirect

Journal of Colloid And Interface Science

journal homepage: www.elsevier.com/locate/jcis

Effect of temperature on the conformation and functionality of poly (*N*-isopropylacrylamide) (PNIPAM)-grafted nanocellulose hydrogels

Vikram Singh Raghuwanshi [a,1], David Joram Mendoza [a,1], Christine Browne [a], Meri Ayurini [b], Gediminas Gervinskas [c], Joel F. Hooper [a,b], Jitendra Mata [d,g], Chun-Ming Wu [d,e], George P. Simon [a,f], Gil Garnier [a]

[a] *Bioresource Processing Research Institute of Australia (BioPRIA), Department of Chemical and Biological Engineering, Monash University, Clayton, Victoria 3800, Australia*
[b] *School of Chemistry, Monash University, Clayton, Victoria 3800, Australia*
[c] *Ramaciotti Centre for Cryo-electron Microscopy, Monash University, Clayton, Victoria 3800, Australia*
[d] *Australian Centre for Neutron Scattering (ACNS), Australian Nuclear Science and Technology Organisation (ANSTO), Lucas Heights, NSW 2234, Australia*
[e] *National Synchrotron Radiation Research Center, Hsinchu 30076, Taiwan*
[f] *Department of Materials Science and Engineering, Monash University, Clayton, Victoria 3800, Australia*
[g] *School of Chemistry, University of New South Wales, Sydney, NSW 2052, Australia*

GRAPHICAL ABSTRACT

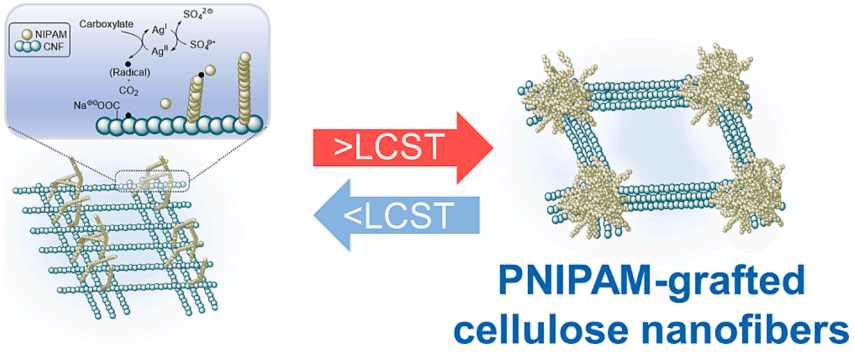

ARTICLE INFO

Keywords:
Poly(*N*-isopropylacrylamide) (PNIPAM)
Grafting
cellulose nanofibers (CNF)
Small angle neutron scattering (SANS)
LCST
Thermo-responsive
Rheology
Ultra small angle neutron scattering (USANS)

ABSTRACT

Hypothesis: Poly(*N*-isopropylacrylamide) [PNIPAM]-grafted cellulose nanofibers (CNFs) are new thermo-responsive hydrogels which can be used for a wide range of applications. Currently, there is no clear understanding of the precise mechanism by which CNFs and PNIPAM interact together. Here, we hypothesize that the physical crosslinking of grafted PNIPAM on CNF inhibits the free movement of individual CNF, which increases the gel strength while sustaining its thermo-responsive properties.
Experiments: The thermo-responsive behaviour of PNIPAM-grafted CNFs (PNIPAM-*g*-CNFs), synthesized *via* silver-catalyzed decarboxylative radical polymerization, and PNIPAM-blended CNFs (PNIPAM-*b*-CNFs) was studied. Small angle neutron scattering (SANS) combined with Ultra-SANS (USANS) revealed the nano to

E-mail addresses: Vikram.raghuwanshi@monash.edu (V.S. Raghuwanshi), gil.ganier@monash.edu (G. Garnier).
[1] *David Joram Mendoza and Vikram Singh Raghuwanshi contributed equally.*

https://doi.org/10.1016/j.jcis.2023.08.152
Received 11 May 2023; Received in revised form 17 August 2023; Accepted 23 August 2023
Available online 24 August 2023
0021-9797/© 2023 The Author(s). Published by Elsevier Inc. This is an open access article under the CC BY-NC-ND license (http://creativecommons.org/licenses/by-nc-nd/4.0/).

microscale conformation changes of these polymer hybrids as a function of temperature. The effect of temperature on the optical and viscoelastic properties of hydrogels was also investigated.
Findings: Grafting PNIPAM from CNFs shifted the lower critical solution temperature (LCST) from 32 °C to 36 °C. Below LCST, the PNIPAM chains in PNIPAM-*g*-CNF sustain an open conformation and poor interaction with CNF, and exhibit water-like behaviour. At and above LCST, the PNIPAM chains change conformation to entangle and aggregate nearby CNFs. Large voids are formed in solution between the aggregated PNIPAM-CNF walls. In comparison, PNIPAM-*b*-CNF sustains liquid-like behaviour below LCST. At and above LCST, the blended PNIPAM phase separates from CNF to form large aggregates which do not affect CNF network and thus PNIPAM-*b*-CNF demonstrates low viscosity. Understanding of temperature-dependent conformation of PNIPAM-*g*-CNFs engineer thermo-responsive hydrogels for biomedical and functional applications.

1. Introduction

Poly(*N*-isopropylacrylamide) (PNIPAM) is a thermo-responsive polymer now used for many applications including drug delivery, tissue engineering, and smart sensors [1–3]. PNIPAM shows a temperature dependent phase change above a lower critical solution temperature (LCST) of 32 °C [4,5] (Scheme 1a). In water at temperatures below LCST, PNIPAM is hydrophilic and adopts an open and extended coil conformation in which the amide groups are able to form hydrogen bonds with water molecules. At temperatures above LCST, the PNIPAM chains become hydrophobic as the hydrophilic amide groups are shielded by the hydrophobic isopropyl-methyl groups, releasing water molecules. As a result, PNIPAM collapses into a compact globular conformation. The large size of these globules renders the PNIPAM suspension turbid and opaque at temperatures above the LCST.

Besides its conceptual promises, pure PNIPAM in water forms gels with poor mechanical properties which limits its applications [6,7]. Blending PNIPAM with other polymers [8], nanoparticles [9] and metal organic frameworks (MOFs) [10] has been a strategy successfully explored to produce composites of improved mechanical and thermo-responsive properties [11]. Of those nanomaterials, cellulose nanofibers (CNF) have recently been investigated for preparing hydrogels as it is a very attractive and sustainable source of low-cost, organic nanomaterial that can be readily functionalised [12,13]. Mixing CNF with PNIPAM produces suspensions with unique and well-defined thermo-responsiveness and improved mechanical properties which are attractive for functional technologies [14,15]. For instance, Wei *et al.* developed CNF/PNIPAM hydrogels by grafting PNIPAM onto CNF by free-radical polymerization. The hydrogels showed improved mechanical properties and thermo responsive behaviour attributed to the rigidness of CNF [6]. Zhang *et al.* produced high strength PNIPAM/CNF aerogels by blending CNF with PNIPAM; the strength of the aerogels was related to PNIPAM acting as a binder to encourage CNF to form denser networks [15]. Coughlin *et al.* also reported that grafting PNIPAM chains onto methylcellulose, a cellulose derivative, promotes the self-assembly of the water-soluble methylcellulose chains [16]. Recently, we have grafted PNIPAM from CNF using a novel one-pot reaction utilizing the silver-promoted radical decarboxylation of TEMPO-oxidized CNFs [17,18]. By varying the $AgNO_3$ concentration, we were able to modulate the degree of functionalization and properties of PNIPAM grafted from CNFs (PNIPAM-*g*-CNFs).

Whilst our latest reported study was able to demonstrate the thermo-responsive behavior of PNIPAM-*g*-CNFs, a clear understanding of the precise mechanism by which CNF and PNIPAM interact together is still

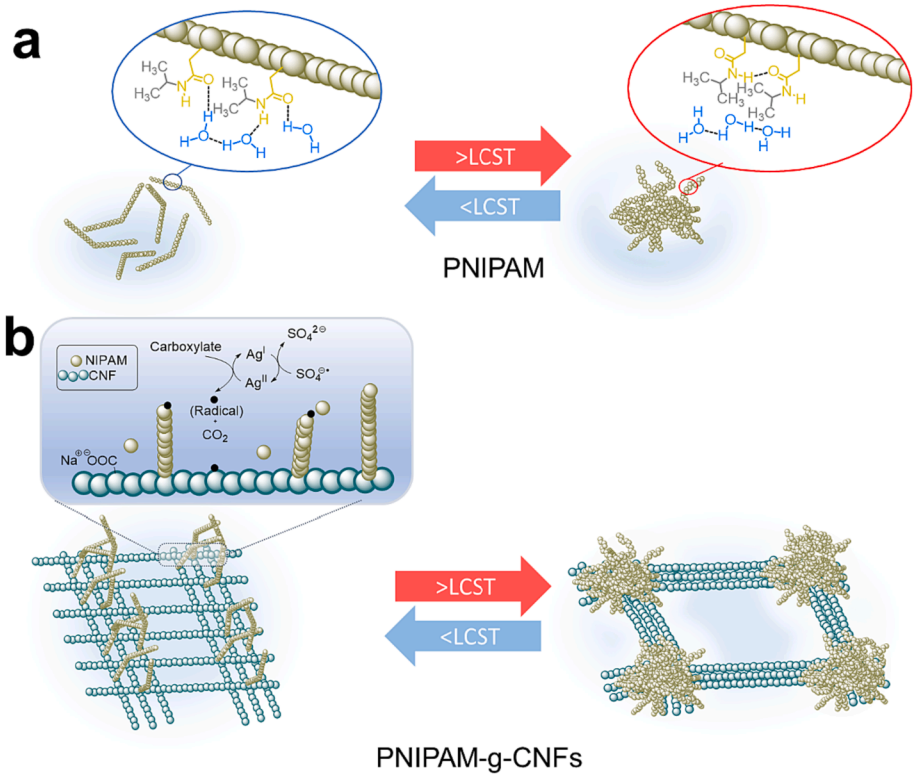

Scheme 1. Schematic illustrating the temperature-dependent behaviour of (a) PNIPAM and (b) PNIPAM-*g*-CNF in water below and above LCST. Inset in (b) illustrates the polymerization of *N*-isopropyl acrylamide (NIPAM) from TEMPO-oxidized CNFs *via* Ag-promoted decarboxylative polymerization.

of importance. Studying how these thermo-responsive macromolecules form well defined structures below and above LCST enables the engineering of functional gels and suspensions systems having the desired LCST and strength. Currently, there are no studies that clearly characterized and defined the structures, interactions, and the transitions mechanisms between PNIPAM and CNF as a function of temperature. Further, little is known on the relationship between structural arrangement of PNIPAM/CNF at the nano to microscale and the gel/suspension mechanical, optical and thermo-responsiveness.

We hypothesize that the PNIPAM chains of these modified nanocellulose aqueous systems can have significant effects on the LCST, mechanical and rheological properties of the suspensions or gels, as well as their degree of swelling and ability to hold water molecules within the matrix [12], whilst at the same time producing improved mechanical properties such as rigidity and strength. In this study, we aim to address three critical questions: 1) Can the LCST of a system be modified and if so, by which variables? 2) Is there a difference in thermal behaviour between blended and grafted systems at a given PNIPAM composition? 3) How do PNIPAM chains and CNF in water interact below and above LCST, and how does it affect the suspensions mechanical properties?

In this work, we investigated the effect of temperature on the conformation and functionality of PNIPAM-grafted CNF (PNIPAM-*g*-CNF) hydrogels we previously prepared *via* silver-promoted decarboxylative polymerization (Scheme 1b). The temperature dependent structural change in PNIPAM-grafted CNF gel is evaluated at temperatures below and above LCST and compared with the CNF, PNIPAM and PNIPAM-blended CNF (PNIPAM-*b*-CNF) gels. Small angle neutron scattering (SANS) is combined with Ultra-SANS (USANS) experiments to monitor the nanoscale and microscale changes in the conformation and arrangement of PNIPAM and CNF in the PNIPAM-*g*-CNF systems. A series of complementary techniques including optical imaging, UV–vis and rheology are used to characterize the optical properties and strength of gels and relate gel properties with their structures. These novel thermo-responsive PNIPAM-grafted CNFs are promising functional materials for application in tissue engineering, smart hydrogels, drug delivery, sensors and bioengineering applications.

2. Experiments

2.1. Materials

All chemicals used were analytical grade and not further purified. *N*-(Carbobenzyloxy)-L-phenylalanine, *N*-isopropylacrylamide (NIPAM), and sodium persulfate ($Na_2S_2O_8$) were purchased from Sigma-Aldrich. Aqueous dispersion (0.82 wt%) of TEMPO-oxidized cellulose nanofibers (TOCNFs) with a carboxylate content of 1.4 mmol COO^-Na^+/g were provided by the University of Maine, USA. Silver nitrate ($AgNO_3$) and acetonitrile (MeCN) were obtained from Merck. D_2O for SANS and USANS experiment was graciously provided by ACNS, ANSTO.

2.2. Synthesis of PNIPAM

N-CBz-phenylalanine (90 mg, 0.30 mmol, 1 equiv), $AgNO_3$ (51 mg, 0.30 mmol, 1 equiv), $Na_2S_2O_8$ (71.5 mg, 0.30 mmol, 1 equiv), and NIPAM (1,698 mg, 15 mmol, 50 equiv) were added to a Schlenk tube and purged with nitrogen gas. Under a nitrogen atmosphere, 5 mL of degassed DMF:water (1:1) was added. The reaction mixture was stirred at 70 °C overnight until > 95% monomer conversion confirmed by ^1H NMR [17]. The crude mixture was diluted with THF and precipitated from diethyl ether 3 times. The resulting polymer was dried under reduced pressure to obtain PNIPAM as a white solid ($M_{n,GPC}$ = 85,500 g/mol; Mw/Mn = 5.27). The gel permeation chromatography (GPC) trace is provided in the supporting information (S1).

2.3. Preparation of PNIPAM-g-CNF and PNIPAM-b-CNF suspensions

PNIPAM-*g*-CNFs were synthesized following a Ag(I)-promoted decarboxylative method we reported previously [17]. In brief, an aqueous suspension of PNIPAM and $Na_2S_2O_8$ in TEMPO-oxidized CNF aqueous dispersion was prepared at 60 °C under N_2. A suspension of $AgNO_3$ in MeCN was added to initiate the reaction at 60 °C for 1 h under N_2. PNIPAM-*g*-CNFs were isolated by repeated washing with water and warm ethanol followed by dialysis against Milli-Q water for 5 days using a regenerated cellulose membrane with a molecular weight cut-off of 12,000 Da. The fibers were then freeze-dried for 2 d and stored at ambient temperature. About 25% of PNIPAM was grafted from CNFs as quantified by TGA and XPS. Aqueous dispersions of PNIPAM-*g*-CNFs (0.5 wt%) were prepared by redispersion in water followed by ultrasonication (Sonics VCX 750) for 5 min. For comparison, 0.5 wt% solution of free PNIPAM was synthesized using a phenylalanine derivative as a source of carboxylic acid. PNIPAM-*b*-CNF (0.5 wt%) suspensions were prepared by adding a known amount of free PNIPAM (25% w/v) to TOCNFs (75% w/v) and stirring for 24 h followed by sonication for 5 min.

2.4. Small -angle neutron scattering (SANS)

Small-angle neutron scattering (SANS) measurements were conducted at the Bilby beamline using Time-of-flight mode at the Australian Centre for Neutron Scattering (ACNS), Australian Nuclear Science and Technology Organisation (ANSTO) [19]. Neutrons with a wavelength range of 2–20 Å ($\Delta\lambda/\lambda$ = 8.3%) were used to cover a q-range from 0.002 to 0.3 $Å^{-1}$. Pure PNIPAM (0.5 wt%), PNIPAM-*g*-CNF (0.5 wt%), and PNIPAM-*b*-CNF (0.5 wt%) dispersed in D_2O were loaded in 2 mm quartz cells and analyzed at 25 °C, 36 °C, and 45 °C. Empty and D_2O-filled cells were used for background scattering correction. Data reduction and normalization to the absolute scattering cross section were performed using home-built Mantid software. The reduced SANS curves were further fitted into the shape dependent form factor model using the SASFit software [20]. Table 1 shows the scattering length density (SLD) and the volume fraction of the suspension.

2.5. Ultra-Small-angle neutron scattering (USANS)

Ultra-Small angle neutron scattering (USANS) measurements were conducted at the Kookaburra beamline at the ACNS, ANSTO using high flux mode with a 4.74 Å wavelength. The suspensions were loaded in 2 mm Kookaburra demountable cells. D_2O-filled cells were used for background scattering correction. Data reduction and normalization to the absolute scattering cross section were performed using the Kookaburra script in a home-built platform GUMTREE [21]. These slits smeared absolute data were further processed (de-smeared) using Python script implemented in Mantid software [22] using the Lake algorithm [22,23] before combining with SANS data.

2.6. UV–VIS spectroscopy

UV–Vis absorption spectroscopy was conducted on the Agilent Cary 3500 Multicell Peltier UV–Vis instrument. The suspensions of CNF, PNIPAM, PNIPAM-*g*-CNF and PNIPAM-*b*-CNF were filled in the quartz cuvettes. Temperature probes are attached to the cuvette to monitor the

Table 1
Scattering length density (SLD) and the volume fraction of TEMPO oxidised CNF and PNIPAM in the suspension.

Sample	SLD x10^{-6} 1/Å^2	Vol fraction (%)
Deuterium	6.33	–
CNF with COO^-	3.77	0.23
PNIPAM	0.81	0.11

suspension temperature during measurements. Absorbance was measured at 600 nm in 0.1 °C interval for a temperature range from 25 to 50 °C at a heating rate of 1 °C/min.

2.7. Rheology

Rheology on the 1 wt% TEMPO oxidized CNF and PNIPAM-*g*-CNFs suspensions was conducted on an Anton Paar MCR302 rheometer. A 25 mm parallel plate geometry was used. The storage (G′) and loss (G″) moduli were recorded at a constant strain of 1% and an angular frequency(ω) of 10 rad/s. The experiments were made at temperature increasing from 25 to 45 °C with a rate of 1 °C/min and 1 °C interval and further cooling back from 45 to 25 °C.

2.8. Cryo-Scanning electron microscopy (Cryo-SEM)

Cryo-Scanning electron microscopy (SEM) was conducted on the PNIPAM-*g*-CNF (0.5 wt%) sample dispersed in H_2O. Two samples were prepared at below and above LCST temperature (25 °C and 45 °C). The samples were poured in the gold coated brass container and were plunge frozen in liquid ethane using an automated EM GP2 freezer (Leica Microsystems) and stored in liquid nitrogen (LN_2) overnight. Next day, samples were loaded onto a VCT500 cryo transfer shuttle (Leica Microsystems) inside a VCM (Leica Microsystems) sample handling station under LN_2 conditions. Then samples were transferred into an ACE600 (Leica Microsystems) freeze fracture and sputter coating machine. Inside the ACE600, samples were kept at −176 °C temperature while being freeze fractured to reveal the internal structure of the prepared samples. After the fracture was completed, the samples were freeze etched at −95 °C for 10 min, to enhance the inner features of samples, by gently sublimating some of the ice away from the surface. After the freeze etching was completed, samples were sputter coated with a 10 nm layer of electrically conductive Au/Pd alloy. Finally, samples were transferred into a NovaNano SEM 450 microscope (Thermo Scientific) using a VCT500 cryo vacuum transfer holder and mounted onto the custom built cryo-stage (Leica Microsystems). SEM imaging was performed using low voltage and current (below 3 kV and below 100 pA) to avoid sample damage and charging.

2.9. Transmission electron microscopy (TEM)

Transmission Electron Microscopy (TEM) was performed on CNF suspension diluted to 0.001%. The suspension was sonicated using an ultrasonic probe at 70% amplitude for 2 min followed by drying on a plasma-cleaned copper grid. The sample was stained with 2% uranyl acetate, air dried, and examined at 200 kV using a FEI Tecnai F20 S-TWIN FEGTEM instrument.

3. Results

3.1. Optical measurements

Fig. 1 shows images and temperature-dependent absorbance of 0.5 wt% PNIPAM, PNIPAM-*b*-CNF, and PNIPAM-*g*-CNF aqueous suspensions below (25 °C) and above LCST (45 °C). The absorbance was measured at a wavelength of 600 nm. Below LCST, all suspensions are transparent and show negligible absorbance indicating the formation of structures smaller than the visible light wavelengths (400–700 nm). The light directly passes through the suspension without being scattered from either the PNIPAM or the CNF chains.

Above LCST, PNIPAM and PNIPAM-*g*-CNF suspensions form gels and become turbid as large structures that scattered light in multiple directions are formed (Fig. 1a). The absorbance of PNIPAM solutions increases to 2.5 at LCST (32 °C) and remains constant at higher temperatures (Fig. 1b). However, the absorbance of PNIPAM-*g*-CNF starts to increase at 36 °C and reaches a plateau of 1.25 around 40 °C. The absorbance at the plateau is nearly half that of bulk PNIPAM. This indicates a shift of the LCST for PNIPAM-*g*-CNF to a higher temperature of 36 °C. This is consistent with previous studies where the addition of hydrophilic molecules shifts the phase transition toward higher temperatures [17,24]. Our previous study [17] also revealed that increasing the amount of PNIPAM grafted from CNFs does not significantly shift the

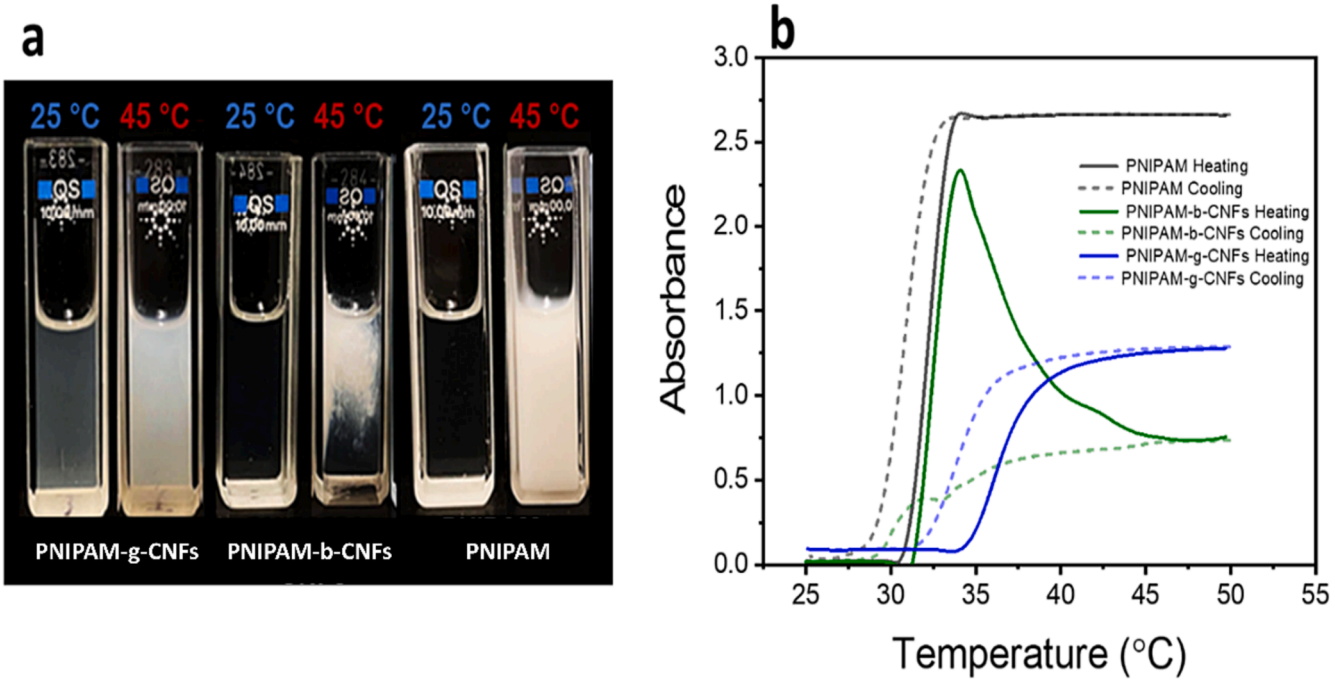

Fig. 1. Effect of thermal transitions on the optical properties of PNIPAM-CNF aqueous systems. (a) Photographs of 0.5 wt% PNIPAM, PNIPAM-*b*-CNFs, and PNIPAM-*g*-CNFs at 25 °C and 45 °C. (b) Temperature-absorbance (600 nm) curves of 0.5 wt% PNIPAM, PNIPAM-*b*-CNFs, and PNIPAM-*g*-CNFs. The temperature range is from 25 °C (below LCST) to 50 °C (above LCST).

LCST.

Above LCST, the PNIPAM-*b*-CNF suspension shows a clear phase separation between CNF and PNIPAM. The bottom of the suspension is partly transparent while the top section is turbid. The absorbance sharply increases at LCST and then decreases to a plateau at 0.5. This abrupt change in absorbance near LCST indicates heterogeneity in the distribution of CNF and PNIPAM chains in the suspension.

3.2. Behaviour of pure PNIPAM and CNF suspensions with temperature

The combination of small angle neutron scattering (SANS) with Ultra-SANS (USANS) uses ideal techniques to assess the temperature-dependent nano- and micro- scale structural changes in the PNIPAM-CNF network. Fig. 2a shows the SANS curves of PNIPAM (0.5 wt%) in D_2O at 3 critical temperatures: below, at and above LCST. The clear differences in the scattering profiles indicate changes in PNIPAM chain conformation below and above LCST. At 25 °C, the power law slope of $q^{-1.0}$ at $q > 0.0025$ Å^{-1} indicates rod-shaped PNIPAM chains [25]. These results confirm the extended coil conformation adopted by PNIPAM chains at room temperature. The slope of q^{-4} at lower q values ($q <$ 0.0025 Å-1: size > 250 nm) originated from the clustering of PNIPAM formed during the preparation along with any entanglement of coils. The high molecular weight and polydispersity of PNIPAM exclude the presence of the structure factor in the SANS intensity [26,27]. Hore *et al.* also observed an upturn in the intensity for the 4% PNIPAM in a deuterated water suspension above 25 °C [28]. This low q region signal originates from the composition fluctuations of phase separation or structural heterogeneities which merges with the signals from intermediate q range signals [27–29]. As temperature increases to 45 °C, the q^{-4} slope starts early at $q < 0.05$ Å^{-1} indicating the formation of compact PNIPAM chain aggregates.

The aqueous CNF (0.5 wt%) suspension shows similar scattering curves at the three temperatures (*25 °C, 36 °C and 45 °C*) tested, indicating its temperature-independent structural arrangements. (Fig. 2b). The q^{-2} slope at higher q values ($q > 0.05$ Å^{-1}) reveals the parallelepiped shape of CNF which is consistent with previous work [30,31]. At intermediate q values ($0.01 < q < 0.045$ Å^{-1}), the slope of q^{-1} shows a linear shape of CNF. However, the slope of $q^{-3.5}$ at lower q value ($q <$ 0.003 Å^{-1}) reveals scattering from the large structure formed by aggregated CNF as shown in the TEM image in the supporting information [S4]. The scattering curve of CNF fits well with the parallelepiped model as well as with the cylinder model. The fitted CNF curve with the parallelepiped model is shown in the supporting information (S2). In both cases, the CNF cross section is about 3 nm × 5 nm,

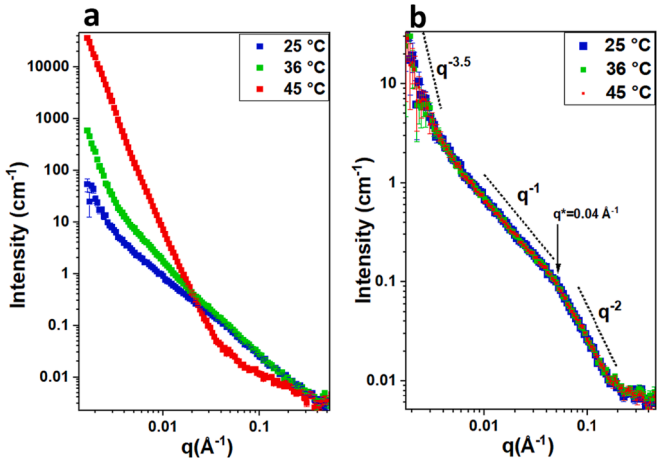

Fig. 2. SANS intensity-versus q vector curves of the individual constituents: (a) PNIPAM in D_2O at different critical temperature. (b) CNF in D_2O at different temperatures: 25 °C, 36 °C, 45 °C.

consistent with literature [31]. The correlation peak (or hump) at $q^* = 0.04$ Å^{-1} gives the inter-fiber distance ('d') of 14 nm calculated by the relation $d = 2pi/q^*$.

3.3. Behaviour of PNIPAM blended with CNF (PNIPAM-b-CNF) with temperature

Fig. 3*a* shows the merged SANS-USANS curves of blended PNIPAM-*b*-CNF, below (25 °C) and above (36 and 45 °C) the LCST of bulk PNIPAM (32 °C). The differences in the scattering profiles indicate a different structural arrangement at 25 °C from those at 36 and 45 °C. Interestingly, the scattering profile at 36 and 45 °C (red and green curve in Fig. 3a) are identical, revealing similar structural arrangement above the PNIPAM LCST.

At 25 °C, the SANS profile of PNIPAM-*b*-CNF is similar to that of the bulk CNF (Fig. 3b). Blending PNIPAM chains has no effect on the mesh structure of CNF suspensions as the free PNIPAM chains entangle between the CNF bonded with weak interactions. The SANS curve of PNIPAM-*b*-CNF fits well with a cylinder model with the rod diameter of 3–5 nm from the CNF. Details of the fitting are provided in the supporting information (S3). The SANS-USANS curves at 36 and 45 °C are similar and show two humps: (i) at higher q value ($q^* = 0.04$ Å^{-1}) SANS region and (ii) at the lower q value ($q^* = 0.00047$ Å^{-1})-USANS region. The hump at high q value is from the CNF mesh structure. However, the hump at the low q range indicates the formation of large structures from the aggregation of PNIPAM chains which have formed compact globules.

These SANS curves fit well with the form factor of a cylinder (diameter 3–5 nm) combined with a sphere (diameter 640 nm). The large sphere represents the aggregate of PNIPAM chains in the CNF network. The interparticle distance between these aggregates is 1350 nm evaluated from the correlation peak at $q^* = 0.00047$ Å^{-1}. The scattering from the spherical structure model contains both the PNIPAM and CNF fractions. Moreover, additional CNF and NIPAM fibers connected with the sphere contribute to the scattering. Thus, it is difficult to determine reliable $I(q = 0)$ to extract the specific composition fraction of NIPAM and CNF in this system. Additionally, the intensity in SANS/USANS region is still going up at low q which indicates that there are structures larger than the size range these techniques cover. This poses difficulty to get volume fraction information. For simplicity, we assumed a simple spherical and cylinder model to fit the SANS-USANS curves without adding further complexity.

3.4. Behaviour of PNIPAM grafted on CNF (PNIPAM-g-CNF) with temperature

Fig. 4a shows the SANS-USANS curves for grafted PNIPAM-*g*-CNF measured below (25 °C), at (36 °C) and above (45 °C) the LCST of PNIPAM-*g*-CNF. The scattering curve of PNIPAM-*g*-CNF at 25 °C shows two correlation humps while PNIPAM-*b*-CNF displays a single hump (Fig. 5a). The first hump (at $q^* = 0.04$ Å^{-1}) in both samples is similar which is from the CNF mesh structure.

At 25 °C, the hump between $0.004 < q < 0.02$ Å^{-1} differs from the CNF scattering curve, revealing scattering from the structural changes due to grafted PNIPAM chains. The hump is centred at $q^* = 0.0097$ Å^{-1} which gives an interparticle distance of 65 nm ± 2 nm. The scattering curve of PNIPAM-*g*-CNF at 25 °C is well fitted by the two cylinders model. The diameter of the smaller cylinder is about 3 nm which corresponds to the CNF diameter. The large cylinders 20 nm in diameter are bundles formed by nearby CNF. The inter spacing between these bundles is 65 nm ± 2 nm.

At LCST (36 °C), the SANS-USANS curve shows an increase in scattering intensity with a broad hump at $q^* = 0.0031$ Å^{-1}. The broadness of this hump reveals a large size distribution of the structures formed and the position of the hump gives an interparticle distance of 200 nm ± 3 nm. Above LCST (45 °C), the SANS-USANS curve shows two clear humps

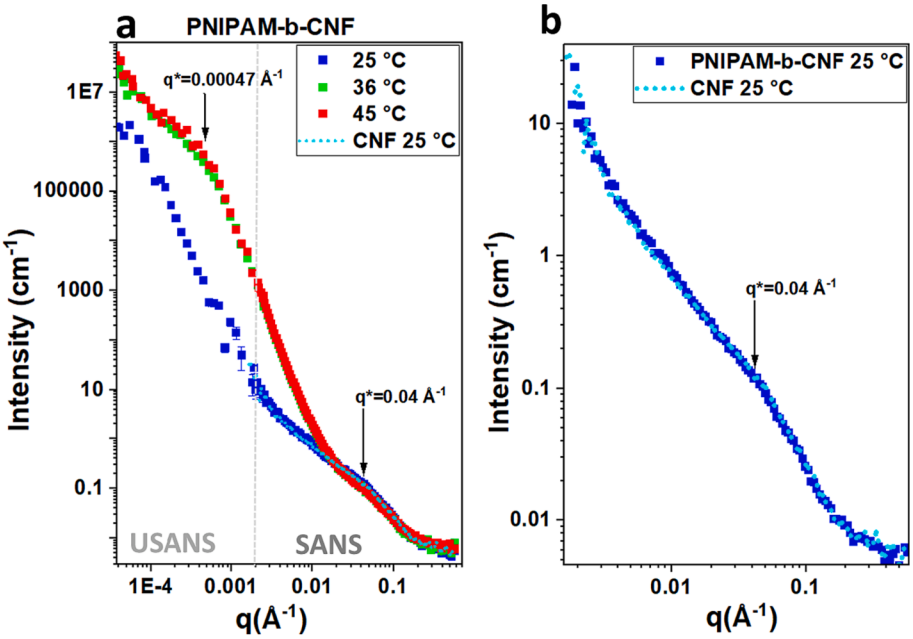

Fig. 3. (a) SANS-USANS curves of the blended systems including PNIPAM-*b*-CNF in D_2O suspension at different temperatures: 25 °C, 36 °C and 45 °C. (b) SANS-USANS curves of PNIPAM-*b*-CNF and CNF in D_2O at 25 °C.

centred at q* = 0.0023 $Å^{-1}$ and 0.0167 $Å^{-1}$. These two humps indicate the formation of homogenous structures and the primary hump at q = 0.0023 $Å^{-1}$ gives an interparticle distances of 290 nm ± 5 nm.

The SANS scattering curves of PNIPAM-*g*-CNF at 36 °C and 45 °C both fit well with the model of a sphere combined with a cylinder. The fitted curve is presented in the supporting information (S4). The cylinder diameter of 3–5 nm at 36 °C is similar to CNF. However, the cylinder diameter increases to 10 nm (at 45 °C) which indicates a growth in the thickness of the CNF due to the conformation change of the corona from the PNIPAM grafted from the CNF surface. The sphere diameter (for 36 °C) is about 50 nm. The spheres are formed by the partly closed structures of PNIPAM chains which are entangled with the CNF. The spaces between these spheres are about 200 nm which corresponds to the void space between CNF entangled by PNIPAM. The sphere diameter (for 45 °C) also increases to 100 nm. The large sphere is formed by the entangled CNF collapsed by the conformation change of the PNIPAM chains. The void spaces between these spheres also increase to about 290 nm.

At 25 °C, the slope of $q^{-1.7}$ in the intermediate q value reveals the open conformation of the PNIPAM chains and CNF fibrils. Increasing temperature to LCST increases the slope to $q^{-2.5}$ indicating the formation of fractals which become more compact above LCST where the slope increases to $q^{-3.1}$. The compactness originates from the closed conformation of grafted PNIPAM and its effect on the nearby CNF.

Cryo-SEM is conducted to visualize the internal structure of the PNIPAM-*g*-CNF gel below and above the LCST temperature (25 and 45 °C) (Fig. 4 c and d). The micrograph for the sample below LCST shows the open structures of the PNIPAM-*g*-CNF. The inset in Fig. 4c clearly reveals that large open structures are formed. However, for the sample above the LCST, better ordered and aligned structures with regular and closed unit cells are observed (Fig. 4d). These results obtained from the real space imaging by cryo-SEM agree well with the SANS-USANS data analysis.

3.5. Comparison of blended and grafted PNIPAM-CNF systems at different temperature

Fig. 5 compares the SANS-USANS curves of PNIPAM-*g*-CNF with PNIPAM-*b*-CNF suspensions at different temperatures. There are noticeable differences as changes in the PNIPAM chains' conformation with temperature lead to different structural arrangements between the blended and grafted PNIPAM- CNF systems.

At 36 °C, the hump at the higher q values in both PNIPAM-*g*-CNF and PNIPAM-*b*-CNF is from the CNF mesh structure. However, the broad hump in the intermediate q values of PNIPAM-*g*-CNF is from the entangled PNIPAM/CNF structure which forms voids of 200 nm. The hump shifts towards the lower q values for the PNIPAM-*b*-CNF indicating the formation of large phase separated structures of aggregated PNIPAM chains.

At 45 °C, the scattering of PNIPAM-*b*-CNF is similar to the blended sample at 36 °C indicating no effect of temperature on phase separated PNIPAM and CNF. However, the SANS curve of PNIPAM-*g*-CNF shows two humps indicating the formation of homogenous size structures separated by a regular and finite distance. The formed structures are the voids which grow to a larger size of 290 nm.

3.6. Rheology

Fig. 6 presents the rheological properties of TEMPO-oxidised CNF, bulk PNIPAM, PNIPAM-*b*-CNF, and PNIPAM-*g*-CNF suspensions. The storage (G') and loss (G'') moduli are quantified as a function of temperature. G' and G'' describe the solid-like and liquid-like behaviour of the material, respectively. The viscoelastic properties of TEMPO-oxidised CNF are not significantly affected by temperature. Bulk PNIPAM, on the other hand, displays higher moduli relative to CNF as shown in Fig. 6b. A significant increase in moduli is observed at 32 °C, with the magnitude of G'' dominating that of G' over almost the full range of temperature tested. PNIPAM-*b*-CNFs shows a similar pattern as bulk PNIPAM with a remarkable increase in G' observed at 32 °C. Interestingly, cooling measurements reveal the viscoelastic behaviour of the PNIPAM-CNF to be irreversible. The PNIPAM-*g*-CNF suspension displays a temperature-dependent sol–gel transition at 36 °C. Below this temperature, G'' is greater than G', showing the PNIPAM-*g*-CNF suspension behaves as a stable sol. However, above 36 ℃, G' becomes dominant over G'' indicating that it has transitioned into a solid-like material.

Table 2 summarizes the G' of CNFs, bulk PNIPAM, PNIPAM-*b*-CNF, and PNIPAM-*g*-CNF at different temperatures. The viscoelastic

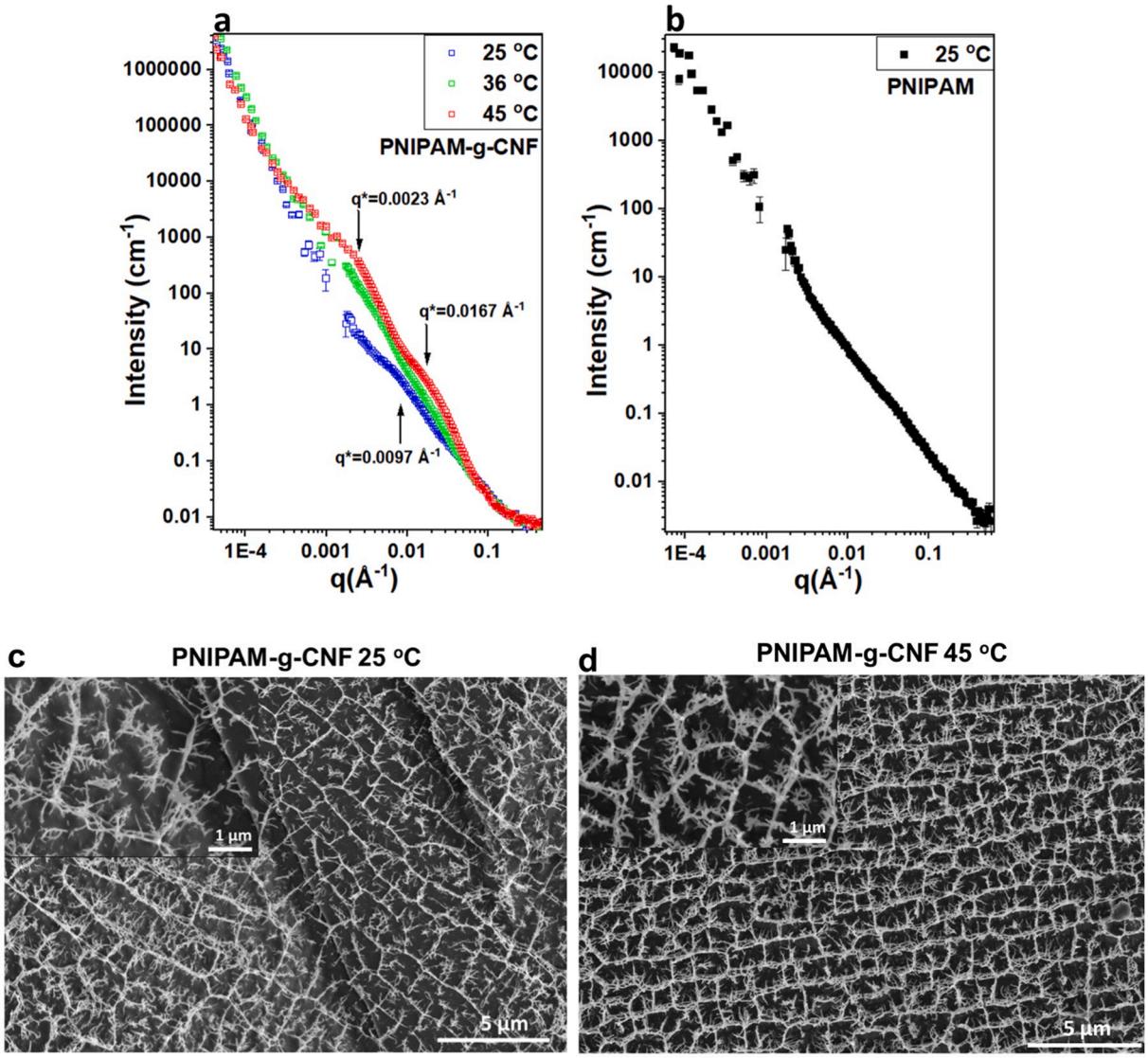

Fig. 4. SANS-USANS curves of (a) grafted PNIPAM-*g*-CNF in the D_2O suspension at different temperatures: 25 °C, 36 °C and 45 °C. (b) SANS-USANS curve of PNIPAM in D_2O at 25 °C. Cryo-Scanning electron microscope (Cryo-SEM) images of (c) PNIPAM-*g*-CNF in the H_2O suspension quenched in liquid ethane from equilibrium at different temperatures (c)25 °C (d) 45 °C. Inset shows the enlarge image.

properties of CNF suspensions are not significantly affected by temperature. Bulk PNIPAM and PNIPAM-*b*-CNFs display similar behaviour: G' increases at 36 °C and slightly decreased at 45 °C. At all temperatures tested, G' of PNIPAM-*b*-CNF is lower than that of PNIPAM. Interestingly, grafting PNIPAM from CNF dramatically increases its storage modulus when heated above its LCST. At 45 °C, a 25-fold increase in G' is observed in PNIPAM-*g*-CNF relative to PNIPAM.

4. Discussion

The temperature-dependent structural changes of the PNIPAM-grafted CNF (PNIPAM-*g*-CNF) gel were evaluated and compared with the bulk PNIPAM and PNIPAM-blended CNF (PNIPAM-*b*-CNF) gels. The structural changes in the system affect both the LCST and the strength of the gel.

Absorbance and rheological measurements reveal an LCST of 32 °C for the bulk PNIPAM which is consistent with previous studies [32,33]. Below LCST (25 °C), PNIPAM aqueous suspensions are transparent (Fig. 1) and demonstrate a liquid-like behaviour in rheology (Fig. 6b). PNIPAM is hydrophilic in water as the amide groups are hydrated by the surrounding water molecules *via* hydrogen bonding [34,35]. Thus, the PNIPAM chain adopts an open coil conformation which contributes to a liquid like behaviour (Fig. 7a). At and above LCST, H-bonds between the amide groups of PNIPAM become energetically more favourable than inter-molecular bonds with surrounding water molecules. This causes new intra- and inter-chain H-bond formation between the amide groups of PNIPAM leading to a change in conformation from coil to globule (Fig. 7a) [35].

Similarity in the scattering curves of blended PNIPAM-*b*-CNF and pristine CNF at room temperature (Fig. 3b) indicates that blending PNIPAM has no effect on the CNF network. In this CNF network, the blended PNIPAM chains have only weak interactions with CNF and do not constrain the CNF structural arrangement. The PNIPAM chains move freely in an open coil conformation as separated entities in the CNF network, producing a free-flowing liquid like suspension. The LCST of PNIPAM-*b*-CNF is similar to that of the bulk PNIPAM which is due to the free movement of the PNIPAM chains. Above the LCST, the PNIPAM-*b*-CNF shows phase separation in the optical images (Fig. 1a). Above LCST, free PNIPAM chains in the CNF network change their conformation to globular, entangle and form large aggregates 640 nm in diameter which are 1350 nm apart (red lines in the Fig. 7b).

In PNIPAM-*g*-CNF suspensions, the thermal transition (LCST 36 °C) is

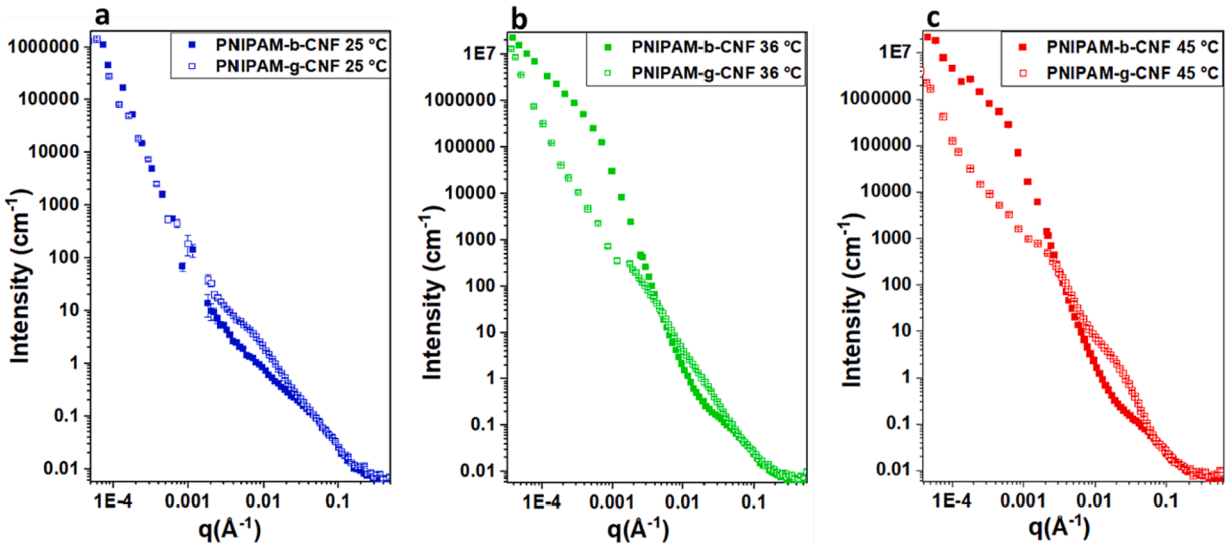

Fig. 5. Comparison of SANS-USANS curves of the blended PNIPAM-*b*-CNF with the grafted PNIPAM-*g*-CNF in D_2O at different temperatures: (a) below 25 °C, (b) at 36 °C and (c) above45 °C LCST.

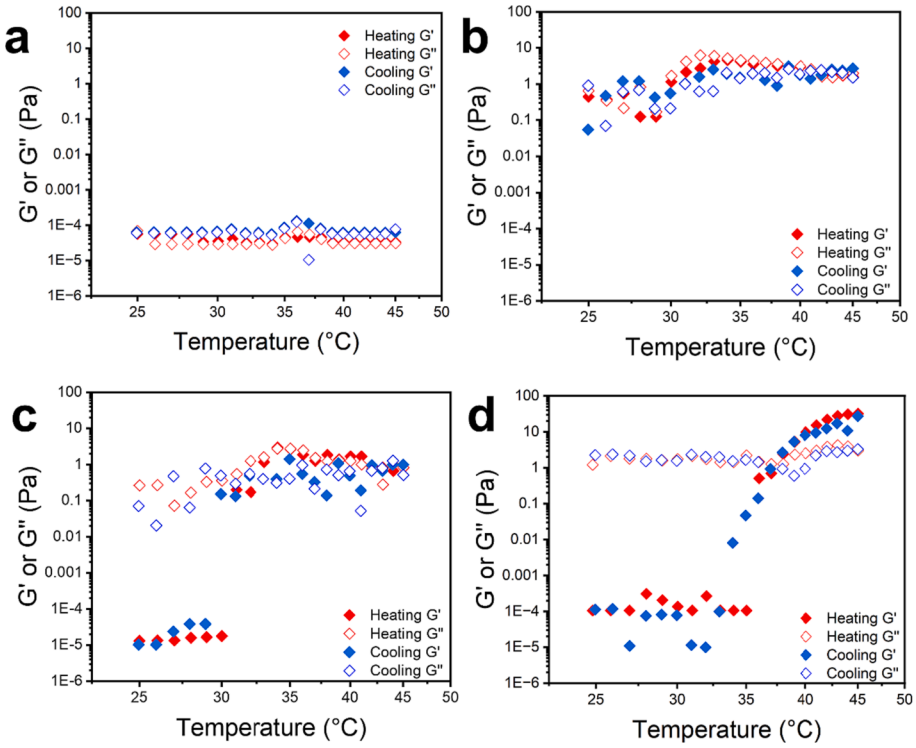

Fig. 6. Temperature dependence of G' (closed symbol) and G'' (open symbol) of 0.5 wt% (a) TEMPO-oxidized CNFs, (b) PNIPAM, (c) blended PNIPAM-*b*-CNFs, and (d) grafted PNIPAM-*g*-CNFs aqueous suspensions. The samples were measured at 1% constant strain and 10 rad/s angular frequency at a heating rate of 1 ℃/min.

Table 2
Storage moduli (G') of 0.5 wt% TEMPO-oxidized CNFs, bulk PNIPAM, PNIPAM-*b*-CNFs, and PNIPAM-g-CNFs at 25 °C, 36 °C, and 45 °C. Measurements were performed at a constant strain of 1%, angular frequency of 10 rad/s, and heating rate of 1 ℃/min.

Sample	Storage modulus, G' (Pa)		
	25 °C	36 °C	45 °C
CNF	5.64×10^{-5}	7.01×10^{-5}	3.29×10^{-5}
PNIPAM	4.48×10^{-5}	3.54	1.56
PNIPAM-*b*-CNF	1.32×10^{-5}	1.86	0.82
PNIPAM-*g*-CNF	6.04×10^{-5}	0.30	38.47

close to the normal human body temperature, providing the potential for this material to be used in functional biomedical applications. The LCST of PNIPAM is highly affected by several polymer properties such as substituent groups, grafting density, molecular weight, and tacticity [36–40]. The shift in LCST is ascribed to the changes in the hydrophobic interactions and hydrogen bonding between PNIPAM and water. In this system, an increase in LCST for PNIPAM-*g*-CNF is driven by the limitations on the PNIPAM chains mobility due to one end immobilized onto the CNF. These new structural measurements support previous work of PNIPAM-grafted cellulose nanocrystals [41,42]. Below the LCST, PNIPAM chains' free-end entangles with the nearby CNF to form smaller

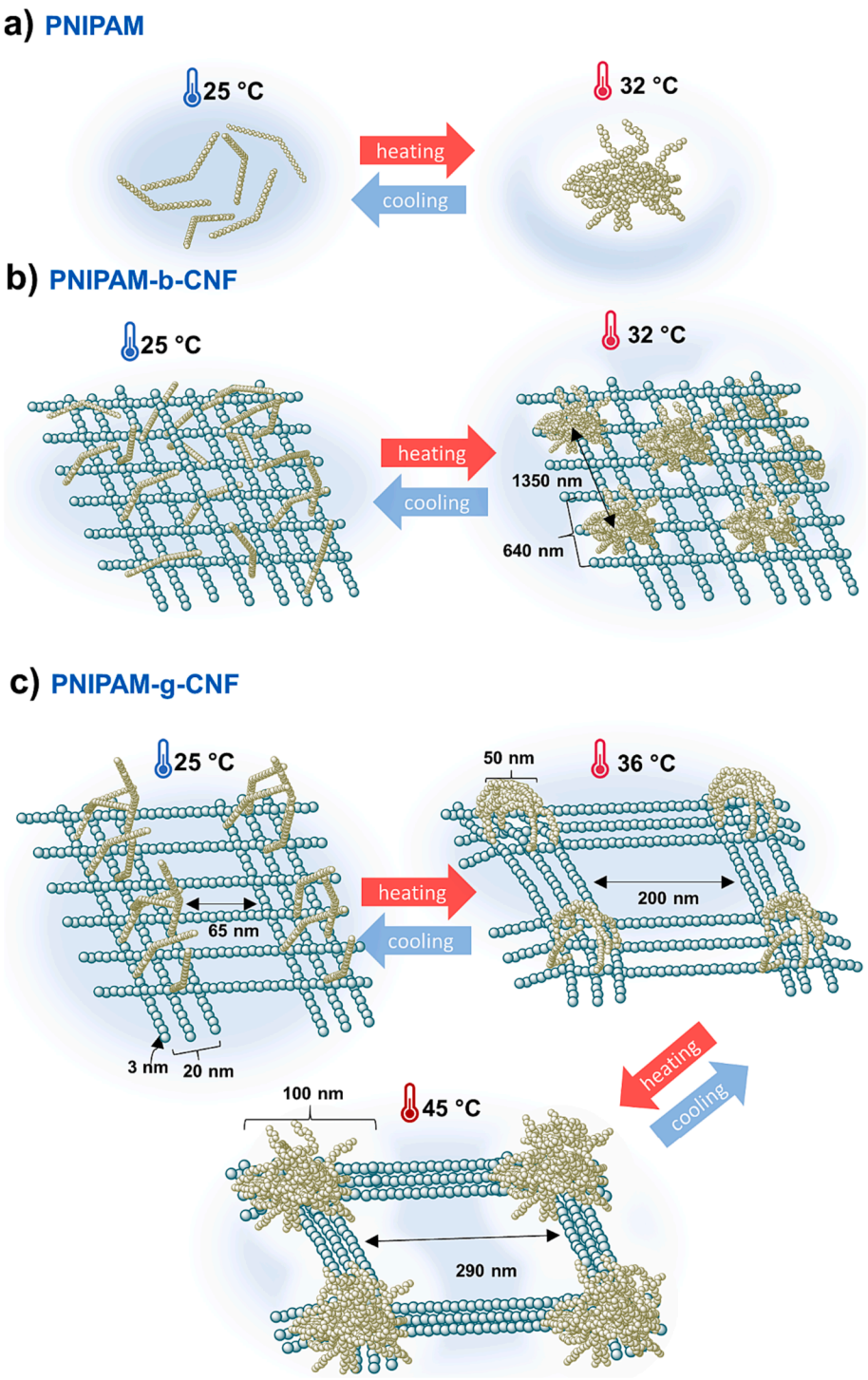

Fig. 7. (a) Schematic mechanism of the PNIPAM conformation below and above LCST. (b) Schematic of the blended PNIPAM-*b*-CNF conformation below and above LCST (c) Schematic of the grafted PNIPAM-*g*-CNF conformation below and above LCST.

and loosely interacting CNF bundles of thickness 20 nm which are 65 nm apart (Fig. 7c). The weak interaction between PNIPAM and CNF in the network creates a free-flowing suspension. At the LCST, the PNIPAM chains change conformation from an open coil towards a collapsing structure. Upon this changing conformation, the PNIPAM chains entangle and become closer to nearby PNIPAM/CNF units also by physical entanglement. As the nearby CNF rods come closer together, they create boundaries with PNIPAM/CNF nodes which are 50 nm thick. The large structures are formed within the suspension by fiber exclusion creating voids 200 nm in size. The multiple visible light scatterings from the CNF/PNIPAM boundaries and voids in all directions make the suspension turbid. Above LCST, the PNIPAM chains dehydrate and collapse completely into a compact globule. These collapsing PNIPAM/CNF bundles form large agglomeration bundles of PNIPAM/CNF nodes 100 nm in size which also increase the void size to 290 nm. These voids and boundaries are homogenous in size, as indicated by the readily observable correlation humps in the SANS. The large structures formed by voids separated by PNIPAM/CNF thick boundaries keep the suspension turbid and opaque.

Above LCST (45 °C), the grafted PNIPAM-*g*-CNF shows a solid-like

gel behaviour with the elastic modulus (G') increased by a factor 25× higher than PNIPAM and 47× higher than the blended PNIPAM-*b*-CNF system. Grafting PNIPAM from CNF significantly increases the strength of the gel, while blending PNIPAM weakens it. The weakness in the PNIPAM-*b*-CNF material may result from the phase separation at higher temperature (Fig. 1a). The weak interaction between aggregated PNIPAM and CNF structures does not support the overall network structure and weakens the gel. However, for the PNIPAM-*g*-CNF, the dense bundle wall of PNIPAM/CNF and the organised void structures increases the gel strength.

5. Conclusion

Inspired by the vast emerging applications of PNIPAM [1–3], we grafted this thermo-responsive polymer from CNFs and studied the effect of temperature on the conformation and functionality of the resulting polymer hybrid. Whilst our previous study [17] showed the efficient grafting of PNIPAM from CNFs, the current study presents a fundamental understanding of temperature dependent nano- and micro-scale structural arrangement due to changes in grafted PNIPAM conformation on CNF. Through SANS-USANS and other complementary analyses, we elucidated the changes in conformation and functionality of a) PNIPAM, b) PNIPAM-grafted CNFs (PNIPAM-*g*-CNFs) and c) PNIPAM-blended CNFs (PNIPAM-*b*-CNFs) as affected by temperature.

Below LCST (25 °C), these suspensions in water all demonstrate a transparent-liquid like behaviour. The hydrophilic PNIPAM remains in an open, extended coil conformation and the weak CNF-PNIPAM interaction leads to a transparent and free flowing suspension. At the LCST, the suspension changes from being free flowing to a gel-like liquid due to the globular conformation of PNIPAM.

In PNIPAM-*b*-CNF gels, above LCST, the free PNIPAM chains collapse, agglomerate and form large size aggregates in the CNF network. The blended PNIPAM chains do not affect CNF mesh structure. The weak interaction between CNF and PNIPAM forms weak gels. The large size of the aggregates leads to multiple light scattering which renders the suspension turbid.

In the PNIPAM-*g*-CNF suspensions, the PNIPAM chains bring the nearby CNFs closer together by physical entanglement at the LCST. As some nearby CNFs come closer, the distance between other CNF units increases which creates large voids 200 nm in size. The entangled PNIPAM-CNF structures form the boundaries of these voids. Above LCST, the PNIPAM chains collapse completely and form a compact globule which entangles further more CNFs and brings them closer together. This further expands the average void size to 290 nm. The resultant voids and PNIPAM/CNF bundle boundaries are homogeneously distributed in suspension, and they inhibit the free movement of PNIPAM and CNF, increasing the gel strength. Gels made from grafted PNIPAM-*g*-CNF are nearly 50 times stronger (as measured with G') than those from blended PNIPAM-*b*-CNF. This phenomenon is reversible upon varying temperature below and above LCST. These new structural measurements support previous work of PNIPAM-g-CNC [41,42]. Grafting PNIPAM from CNF increases the LCST from 32 to 36 °C. The grafting process covalently links the PNIPAM with the CNFs, which constrains the movement of the PNIPAM chains in the network. Thus, for the PNIPAM chains to aggregate above the LCST, the CNFs must move to create denser bundles and voids. The energetic penalty of this reorganization is likely responsible for the increase in LCST observed.

As PNIPAM-*g*-CNFs have an LCST close to human body temperature, applications in the biomedical field can be explored. The temperature-dependent conformation of PNIPAM chains grafted on CNF at different pH and salt concentrations can be further studied. This would allow the manipulation of the thermosensitive behaviour of grafted PNIPAM-*g*-CNF hydrogels with varying gel structure, strength and gelation temperature. These are important variables for biomedical applications such as organoids culture [43], drug delivery, smart sensing and tissue engineering.

CRediT authorship contribution statement

Vikram Singh Raghuwanshi: Investigation, Data curation, Formal analysis, Conceptualization, Methodology, Writing – original draft. **David Joram Mendoza:** Investigation, Data curation, Formal analysis, Conceptualization, Methodology, Writing – original draft. **Meri Ayurini:** Investigation, Data curation, Formal analysis, Methodology, Writing – original draft. **Gediminas Gervinskas:** Investigation, Formal analysis, Methodology, Writing – original draft, Conduct Cryo-Scanning Electron Microscopy. **Joel F. Hooper:** Supervision, Conceptualization, Investigation, Writing – review & editing. **Jitendra Mata:** Investigation, Formal analysis, Methodology, SANS Measurements, Analysis. **Chun-Ming Wu:** Investigation, Formal analysis, Methodology, SANS Measurements, Analysis. **George P. Simon:** Supervision, Conceptualization, Investigation, Writing – review & editing. **Gil Garnier:** Supervision, Conceptualization, Funding acquisition, Investigation, Writing – review & editing.

Declaration of Competing Interest

The authors declare that they have no known competing financial interests or personal relationships that could have appeared to influence the work reported in this paper.

Data availability

Data will be made available on request.

Acknowledgements

The authors would like to acknowledge the Australian Research Council (ARC) - Industrial Transformation Hub Grant IH170100020. The authors thank the Australian Nuclear Science and Technology Organisation (ANSTO) for the beamtime (Proposal ID:P14196). The authors acknowledge assistance and support of A/Prof. Georg Ramm as well as the use of instruments at the Monash Ramaciotti Centre for Cryo-Electron Microscopy, a Node of Microscopy Australia. The authors also acknowledge the use of the instruments and scientific and technical assistance of Dr. Tim Williams at the Monash Centre for Electron Microscopy, a Node of Microscopy Australia. This research used FEI Tecnai G2 F20 S-TWIN FEGTEM funded by ARC Grant LE110100223.

Appendix A. Supplementary data

Supplementary data to this article can be found online at https://doi.org/10.1016/j.jcis.2023.08.152.

References

[1] M. Karimi, P.S. Zangabad, A. Ghasemi, M. Amiri, M. Bahrami, H. Malekzad, H. G. Asl, Z. Mandieh, M. Bozorgomid, A. Ghasemi, M.R.R.T. Boyuk, M.R. Hamblin, Temperature-responsive smart nanocarriers for delivery of therapeutic agents: Applications and recent advances, Acs Appl Mater Inter 8 (33) (2016) 21107–21133.

[2] M.A.C. Stuart, W.T.S. Huck, J. Genzer, M. Muller, C. Ober, M. Stamm, G. B. Sukhorukov, I. Szleifer, V.V. Tsukruk, M. Urban, F. Winnik, S. Zauscher, I. Luzinov, S. Minko, Emerging applications of stimuli-responsive polymer materials, Nat. Mater. 9 (2) (2010) 101–113.

[3] Y. Hiruta, Poly(N-isopropylacrylamide)-based temperature- and pH-responsive polymer materials for application in biomedical fields, Polym. J. 54 (12) (2022) 1419–1430.

[4] R. Moerkerke, R. Koningsveld, H. Berghmans, K. Dusek, K. Solc, Phase-transitions in swollen networks, Macromolecules 28 (4) (1995) 1103–1107.

[5] M. Heskins, J.E. Guillet, Solution Properties of Poly(N-isopropylacrylamide), J. Macromol. Sci. A 2 (8) (1968) 1441–1455.

[6] J. Wei, Y. Chen, H. Liu, C. Du, H. Yu, Z. Zhou, Thermo-responsive and compression properties of TEMPO-oxidized cellulose nanofiber-modified PNIPAm hydrogels, Carbohydr. Polym. 147 (2016) 201–207.

[7] M.A. Haq, Y. Su, D. Wang, Mechanical properties of PNIPAM based hydrogels: A review, Mater. Sci. Eng. C 70 (2017) 842–855.

[8] Y. Zhao, C. Shi, X. Yang, B. Shen, Y. Sun, Y. Chen, X. Xu, H. Sun, K. Yu, B. Yang, Q. Lin, pH- and temperature-sensitive hydrogel nanoparticles with dual photoluminescence for bioprobes, ACS Nano 10 (6) (2016) 5856–5863.
[9] S.T. Jones, Z. Walsh-Korb, S.J. Barrow, S.L. Henderson, J. del Barrio, O. A. Scherman, The importance of excess poly(N-isopropylacrylamide) for the aggregation of poly(N-isopropylacrylamide)-coated gold nanoparticles, ACS Nano 10 (3) (2016) 3158–3165.
[10] A. Karmakar, P.G.M. Mileo, I. Bok, S.B. Peh, J. Zhang, H. Yuan, G. Maurin, D. Zhao, Thermo-responsive MOF/Polymer composites for temperature-mediated water capture and release, Angew. Chem. Int. Ed. 59 (27) (2020) 11003–11009.
[11] C. Sun, D. Zhu, H. Jia, K. Lei, Z. Zheng, X. Wang, Humidity and heat dual response cellulose nanocrystals/poly(N-Isopropylacrylamide) composite films with cyclic performance, Acs Appl Mater Inter 11 (42) (2019) 39192–39200.
[12] A. Hebeish, S. Farag, S. Sharaf, T.I. Shaheen, Thermal responsive hydrogels based on semi interpenetrating network of poly(NIPAm) and cellulose nanowhiskers, Carbohyd. Polym. 102 (2014) 159–166.
[13] L. Hossain, V.S. Raghuwanshi, J. Tanner, G. Garnier, Modulating nanocellulose hydrogels and cryogels strength by crosslinking and blending, Colloids & Surf A Physicochem Eng Asp 630 (2021) 127608.
[14] F. Zhang, W. Wu, X. Zhang, X. Meng, G. Tong, Y. Deng, Temperature-sensitive poly-NIPAm modified cellulose nanofibril cryogel microspheres for controlled drug release, Cellul. 23 (1) (2016) 415–425.
[15] X. Zhang, Y. Wang, J. Zhao, M. Xiao, W. Zhang, C. Lu, Mechanically strong and thermally responsive cellulose nanofibers/poly(N-isopropylacrylamide) composite aerogels, ACS Sustain. Chem. Eng. 4 (8) (2016) 4321–4327.
[16] M.L. Coughlin, J. Edmund, F.S. Bates, T.P. Lodge, Temperature dependence of chain conformations and fibril formation in solutions of Poly(N-isopropylacrylamide)-grafted methylcellulose, Macromolecules 55 (2) (2022) 550–558.
[17] D.J. Mendoza, M. Ayurini, C. Browne, V.S. Raghuwanshi, G.P. Simon, J.F. Hooper, G. Garnier, Thermoresponsive Poly(N-isopropylacrylamide) grafted from cellulose nanofibers via silver-promoted decarboxylative radical polymerization, Biomacromolecules 23 (4) (2022) 1610–1621.
[18] D.J. Mendoza, M. Ayurini, V.S. Raghuwanshi, G.P. Simon, J.F. Hooper, G. Garnier, Synthesis of superabsorbent polyacrylic acid-grafted cellulose nanofibers via silver-promoted decarboxylative radical polymerization, Macromolecules 56 (10) (2023) 3497–3506.
[19] A. Sokolova, A.E. Whitten, L. de Campo, J. Christoforidis, A. Eltobaji, J. Barnes, F. Darmann, A. Berry, Performance and characteristics of the BILBY time-of-flight small-angle neutron scattering instrument, J. Appl. Cryst. 52 (2019) 1–12.
[20] I. Bressler, J. Kohlbrecher, A.F. Thunemann, SASfit: A tool for small-angle scattering data analysis using a library of analytical expressions, J. Appl. Cryst. 48 (2015) 1587–1598.
[21] C. Rehm, L. de Campo, A. Brûlé, F. Darmann, F. Bartsch, A. Berry, Design and performance of the variable-wavelength bonse-hart ultra-small-angle neutron scattering diffractometer KOOKABURRA at ANSTO, J. Appl. Cryst. 51 (1) (2018) 1–8.
[22] O. Arnold, J.C. Bilheux, J.M. Borreguero, A. Buts, S.I. Campbell, L. Chapon, M. Doucet, N. Draper, R. Ferraz Leal, M.A. Gigg, V.E. Lynch, A. Markvardsen, D. J. Mikkelson, R.L. Mikkelson, R. Miller, K. Palmen, P. Parker, G. Passos, T. G. Perring, P.F. Peterson, S. Ren, M.A. Reuter, A.T. Savici, J.W. Taylor, R.J. Taylor, R. Tolchenov, W. Zhou, J. Zikovsky, Mantid—Data analysis and visualization package for neutron scattering and μ SR experiments, Nuclear instruments and methods in physics research section A: Accelerators, Spectrometers, Detectors and Associated Equipment 764 (2014) 156–166.
[23] J.A. Lake, An iterative method of slit-correcting small angle X-ray data, Acta Crystallogr. 23 (1967) 191–1000.
[24] M. Radecki, J. Spěváček, A. Zhigunov, Z. Sedláková, L. Hanyková, Temperature-induced phase transition in hydrogels of interpenetrating networks of poly(N-isopropylacrylamide) and polyacrylamide, Eur. Polym. J. 68 (2015) 68–79.
[25] L. Hossain, V.S. Raghuwanshi, J. Tanner, C.M. Wu, O. Kleinerman, Y. Cohen, G. Garnier, Structure and swelling of cross-linked nanocellulose foams, J. Colloid Interf. Sci. 568 (2020) 234–244.
[26] B.J. Gold, W. Pyckhout-Hintzen, A. Wischnewski, A. Radulescu, M. Monkenbusch, J. Allgaier, I. Hoffmann, D. Parisi, D. Vlassopoulos, D. Richter, Direct assessment of tube dilation in entangled polymers, Phys. Rev. Lett. 122 (8) (2019) 088001.
[27] M. Shibayama, T. Tanaka, C.C. Han, Small angle neutron scattering study on poly (N-isopropyl acrylamide) gels near their volume-phase transition temperature, J. Chem. Phys. 97 (9) (1992) 6829–6841.
[28] M.J.A. Hore, B. Hammouda, Y. Li, H. Cheng, Co-nonsolvency of poly(n-isopropylacrylamide) in deuterated water/ethanol mixtures, Macromolecules 46 (19) (2013) 7894–7901.
[29] A. Fernández-Barbero, A. Fernández-Nieves, I. Grillo, E. López-Cabarcos, Structural modifications in the swelling of inhomogeneous microgels by light and neutron scattering, Phys. Rev. E 66 (5) (2002) 051803.
[30] V.S. Raghuwanshi, C. Browne, W. Batchelor, G. Garnier, Self-assembly of cellulose nanocrystals of different lengths, J. Colloid Interf. Sci. 630 (2023) 249–259.
[31] T. Rosén, H. He, R. Wang, C. Zhan, S. Chodankar, A. Fall, C. Aulin, P.T. Larsson, T. Lindström, B.S. Hsiao, Cross-sections of nanocellulose from wood analyzed by quantized polydispersity of elementary microfibrils, ACS Nano 14 (12) (2020) 16743–16754.
[32] A. Halperin, M. Kröger, F.M. Winnik, Poly(N-isopropylacrylamide) phase diagrams: Fifty years of research, Angew. Chem. Int. Ed. 54 (51) (2015) 15342–15367.
[33] I. Bischofberger, V. Trappe, New aspects in the phase behaviour of poly-N-isopropyl acrylamide: Systematic temperature dependent shrinking of PNiPAM assemblies well beyond the LCST, Sci. Rep. 5 (1) (2015) 15520.
[34] Y. Ono, T. Shikata, Hydration and dynamic behavior of Poly(N-isopropylacrylamide)s in aqueous solution: A sharp phase transition at the lower critical solution temperature, J. Am. Chem. Soc. 128 (31) (2006) 10030–10031.
[35] M.H. Futscher, M. Philipp, P. Müller-Buschbaum, A. Schulte, The role of backbone hydration of poly(N-isopropyl acrylamide) across the volume phase transition compared to its monomer, Sci. Rep. 7 (1) (2017) 17012.
[36] K.N. Plunkett, X. Zhu, J.S. Moore, D.E. Leckband, PNIPAM chain collapse depends on the molecular weight and grafting density, Langmuir 22 (9) (2006) 4259–4266.
[37] K. Van Durme, G. Van Assche, B. Van Mele, Kinetics of demixing and remixing in poly(N-isopropylacrylamide)/water studied by modulated temperature DSC, Macromolecules 37 (25) (2004) 9596–9605.
[38] M.T. Cook, P. Haddow, S.B. Kirton, W.J. McAuley, Polymers exhibiting lower critical solution temperatures as a route to thermoreversible gelators for healthcare, Adv. Funct. Mater. 31 (8) (2021) 2008123.
[39] T.E. de Oliveira, D. Mukherji, K. Kremer, P.A. Netz, Effects of stereochemistry and copolymerization on the LCST of PNIPAm, J. Chem. Phys. 146 (3) (2017) 034904.
[40] B. Ray, Y. Okamoto, M. Kamigaito, M. Sawamoto, K.-I. Seno, S. Kanaoka, S. Aoshima, Effect of tacticity of Poly(N-isopropylacrylamide) on the phase separation temperature of its aqueous solutions, Polym. J. 37 (3) (2005) 234–237.
[41] K. Zubik, P. Singhsa, Y. Wang, H. Manuspiya, R. Narain, Thermo-Responsive Poly (N-Isopropylacrylamide)-Cellulose Nanocrystals Hybrid Hydrogels for Wound Dressing, Polymers 9 (4) (2017) 119.
[42] J. Wei, Y. Chen, H. Liu, C. Du, H. Yu, J. Ru, Z. Zhou, Effect of surface charge content in the TEMPO-oxidized cellulose nanofibers on morphologies and properties of poly(N-isopropylacrylamide)-based composite hydrogels, Ind. Crop Prod. 92 (2016) 227–235.
[43] R. Curvello, G. Kerr, D.J. Micati, W.H. Chan, V.S. Raghuwanshi, J. Rosenbluh, H. E. Abud, G. Garnier, Engineered plant-based nanocellulose hydrogel for small intestinal organoid growth, Adv. Sci. 8 (1) (2021) 2002135.